photonics

MDPI

Article

Time-Domain and Phase-Resolved Characterization of Partial Discharge Signals Based on Rydberg-Atom Sensing

Haofeng Zhang [1,2,†], Jianjun Chen [3,4,†], Hao Zhang [3,4,*], Bing Luo [1,2,*], Wenguang Yang [3,4], Mingyong Jing [3,4], Zongkai Liu [3,4], Junyao Xie [3,4], Liantuan Xiao [3,4], Suotang Jia [3,4] and Linjie Zhang [3,4]

1 National Engineering Research Center of UHV Technology and Novel Electrical Equipment Basis, China Southern Power Grid, Guangzhou 510000, China; zhanghf2@csg.cn
2 Electric Power Research Institute, China Southern Power Grid, Guangzhou 510000, China
3 State Key Laboratory of Quantum Optics Technologies and Devices, Shanxi University, Taiyuan 030006, China; chenjianjun1@sxu.edu.cn (J.C.); ywg@sxu.edu.cn (W.Y.); jmy@sxu.edu.cn (M.J.); lzk1997@sxu.edu.cn (Z.L.); xiejy@sxu.edu.cn (J.X.); xlt@sxu.edu.cn (L.X.); tjia@sxu.edu.cn (S.J.); zlj@sxu.edu.cn (L.Z.)
4 Collaborative Innovation Center of Extreme Optics, Shanxi University, Taiyuan 030006, China
* Correspondence: haozhang@sxu.edu.cn (H.Z.); luobing@csg.cn (B.L.)
† These authors contributed equally to this work.

Abstract

Rydberg atoms enable sensitive electric-field measurements by converting field-induced changes in atomic energy levels into optically detectable signals. This work investigates four partial discharge models using Rydberg-atom sensing, a commercial ultrahigh-frequency (UHF) antenna, and a custom-built monopole antenna. The measured time-domain signals and phase-resolved partial discharge (PRPD) patterns are compared to evaluate their temporal features and phase-dependent distributions. Particular emphasis is placed on the contribution of atomic sensing to resolving low-frequency components of discharge signals, providing information complementary to conventional UHF measurements. By linking time-domain observations with PRPD characteristics, this study explores the potential of Rydberg-atom sensing to extend the spectral information available for partial discharge characterization.

Keywords: Rydberg-atom sensing; partial discharge; Rydberg electrometry; UHF detection; monopole antenna; PRPD patterns; electromagnetic signal characterization

1. Introduction

Partial discharge (PD) is an important indicator of insulation degradation in high-voltage electrical equipment [1]. Persistent discharge activity can accelerate insulation deterioration and may eventually lead to insulation breakdown and equipment failure [2–5]. Therefore, reliable PD measurement and characteristic analysis are important for assessing insulation conditions and supporting the safe operation of power systems.

Based on the physical signals generated by partial discharge and the corresponding detection principles, existing partial discharge detection methods mainly include electrical, electromagnetic, acoustic, optical, and chemical methods [4,6,7]. Among these, the pulse current method is a traditional and well-established approach [4,8], while electromagnetic-radiation-based methods, such as ultrahigh-frequency (UHF) detection, have also been widely applied to partial discharge detection and online monitoring [7,9]. For electromagnetic detection, the transient electromagnetic signals generated by partial discharge exhibit broadband characteristics, and their radiation and propagation properties are influenced

Check for updates

Received: 8 October 2026
Revised: 23 October 2026
Accepted: 27 October 2026
Published: 28 October 2026

Copyright: © 2026 by the authors. Licensee MDPI, Basel, Switzerland. This article is an open access article distributed under the terms and conditions of the Creative Commons Attribution (CC BY) license.

by factors such as the discharge type, equipment structure, and propagation path [10,11]. Previous studies have shown that partial discharge electromagnetic radiation can extend across broad frequency ranges, including the high-frequency (HF), very-high-frequency (VHF), and UHF bands [12–14]. However, compared with studies covering these frequency ranges, studies on low-frequency electromagnetic responses in the kHz range are still relatively limited. Whether partial discharge exhibits detectable electromagnetic responses in this frequency range and what characteristics such signals have remain to be further investigated. Therefore, extending the spectral range for detecting partial discharge electromagnetic signals and exploring low-frequency electromagnetic responses in the kHz range may provide additional insight into the electromagnetic radiation characteristics of partial discharge.

Rydberg-atom-based quantum electric-field sensing provides a new approach for measuring the transient electromagnetic signals associated with PD. Rydberg atoms exhibit high electric-field sensitivity and a broadband response extending from DC to the terahertz range [15–18]. When an external electric field interacts with highly excited Rydberg atoms, it induces Stark shifts or Autler–Townes (AT) splitting of the atomic energy levels. These changes can be optically detected through electromagnetically induced transparency (EIT) spectroscopy [16], converting local electric-field variations into measurable optical signals and enabling noninvasive electric-field measurements. The measurement can also be traced to fundamental physical constants, reducing the reliance on calibration with conventional antennas [16]. In recent years, Rydberg-atom sensing has attracted increasing attention for radio-frequency and microwave electric-field measurements [19–22], and recent studies have also applied it to the detection of PD signals [23–25]. Compared with conventional electromagnetic sensing methods that primarily target specific frequency bands, the broadband response of Rydberg atoms provides the possibility of capturing additional frequency information from PD signals. It may therefore complement existing UHF and high-frequency detection methods and provide additional information for the characterization of PD electromagnetic signals.

Based on this, we use a Rydberg-atom sensor, a commercial UHF sensor, and a custom-built monopole antenna to measure four types of PD under the same experimental conditions. By comparing the time-domain signals and phase-resolved partial discharge (PRPD) patterns [26–29] obtained with the three sensors, we characterize their responses to the transient and phase-resolved features of different PD types. For the Rydberg-atom sensor, the measured signals are further processed using a 100 kHz low-pass filter to examine its response to lower-frequency information contained in PD signals. This comparison helps assess the role of Rydberg-atom sensing in PD electromagnetic signal characterization and its complementarity with conventional electromagnetic sensing.

2. Rydberg-Atom Sensing Principle

The Rydberg-atom sensor converts an external electric field into an optical transmission response through a ladder-type electromagnetically induced transparency (EIT) system. We consider a three-level atomic system consisting of the ground state $|g\rangle$, intermediate state $|e\rangle$, and Rydberg state $|r\rangle$. A weak probe field couples the $|g\rangle \leftrightarrow |e\rangle$ transition, while a stronger coupling field drives the $|e\rangle \leftrightarrow |r\rangle$ transition. Under the rotating-wave approximation, the interaction Hamiltonian is given by

$$\frac{H}{\hbar} = \frac{1}{2}\begin{pmatrix} 0 & \Omega_p & 0 \\ \Omega_p & -2\Delta_p & \Omega_c \\ 0 & \Omega_c & -2(\Delta_p + \Delta_c) \end{pmatrix}, \quad (1)$$

where Ω_p and Ω_c denote the Rabi frequencies of the probe and coupling fields, respectively, and Δ_p and Δ_c are their corresponding single-photon detunings. The quantity $\Delta_p + \Delta_c$ represents the two-photon detuning and determines the resonance condition involving the Rydberg state.

In the weak-probe regime, the optical response of the atomic system can be described by the probe-transition coherence. Under steady-state conditions, the coherence ρ_{ge} can be expressed as

$$\rho_{ge} = \frac{i\Omega_p}{2}\left[\gamma_{ge} - i\Delta_p + \frac{\Omega_c^2/4}{\gamma_{gr} - i(\Delta_p + \Delta_c)}\right]^{-1}, \tag{2}$$

where γ_{ge} and γ_{gr} are the coherence decay rates. This expression shows that the probe response depends on the two-photon detuning. Near two-photon resonance, the coupling field suppresses probe absorption and produces an EIT transmission feature. Therefore, a shift of the Rydberg-state energy changes the two-photon resonance condition and can be detected through the corresponding variation in probe transmission.

For the thermal atomic ensemble used in the experiment, the atomic velocity distribution introduces Doppler broadening. Because the probe and coupling fields counter-propagate, the velocity-dependent detunings can be written as

$$\Delta_p(v) = \Delta_p - k_p v, \qquad \Delta_c(v) = \Delta_c + k_c v, \tag{3}$$

where k_p and k_c denote the magnitudes of the wavevectors of the probe and coupling fields, respectively. The corresponding two-photon detuning therefore contains a residual velocity-dependent term $(k_c - k_p)v$. The ensemble response can be obtained by averaging the atomic coherence over the velocity distribution,

$$\left\langle \rho_{ge} \right\rangle = \int_{-\infty}^{+\infty} \rho_{ge}(v) f(v)\, \mathrm{d}v, \tag{4}$$

where $f(v)$ denotes the normalized thermal velocity distribution. The probe absorption is proportional to the imaginary part of the atomic susceptibility, which is determined by the ensemble-averaged coherence, and the probe transmission follows from the resulting absorption. Thus, changes in the Rydberg-state energy can be converted into measurable variations in the transmitted probe power.

The PD electric field perturbs the Rydberg state through the Stark effect. In the quadratic Stark regime, the energy shift of the Rydberg state can be written as

$$\Delta W = -\frac{1}{2}\alpha E^2, \tag{5}$$

where E is the external electric-field amplitude and α is the polarizability of the Rydberg state. The corresponding angular-frequency shift is given by

$$\delta\omega_{\mathrm{Stark}} = \frac{\Delta W}{\hbar} = -\frac{\alpha E^2}{2\hbar}. \tag{6}$$

The Stark shift changes the Rydberg-state resonance and consequently modifies the two-photon detuning. With the detuning convention used in the Hamiltonian above, this effect can be represented as

$$\Delta_p + \Delta_c \rightarrow \Delta_p + \Delta_c - \delta\omega_{\mathrm{Stark}}. \tag{7}$$

Therefore, the transient electric field generated by a PD event produces a time-dependent Stark shift, which perturbs the EIT resonance and changes the probe transmission. The photodetector converts this optical transmission variation into an electrical signal. The recorded temporal response thus provides an optical readout of the transient electric field associated with the PD event. In this way, the Rydberg-atom sensor establishes an optical-to-electrical transduction pathway from the PD electric field to the experimentally measured signal.

3. Experimental Setup

3.1. Optical Setup

The experimental optical setup is shown in Figure 1. We use a ladder-type three-level system of Cs atoms, with the 852 nm probe laser driving the $6S_{1/2} \rightarrow 6P_{3/2}$ transition and the 510 nm coupling laser driving the $6P_{3/2} \rightarrow 64D_{5/2}$ transition. The two laser beams first pass through polarization beam splitters (PBSs) for polarization purification and then through half-wave plates (HWPs) to adjust their polarization directions, giving the two beams the same polarization state. The two beams then propagate in a counter-propagating and collinear configuration through the atomic vapor cell. The 852 nm probe beam has a Gaussian beam diameter of approximately 400 μm and a power of 70 μW, while the 510 nm coupling beam has a Gaussian beam diameter of approximately 450 μm and a power of 30 mW. A small fraction of the probe light is reflected from a white glass plate for probe-power stabilization, thereby reducing the influence of laser-power fluctuations on the measurements. Both lasers use the Pound–Drever–Hall (PDH) technique [30] for frequency stabilization and are locked to frequencies that satisfy the two-photon EIT resonance condition, with locking bandwidths of 250 kHz and 700 kHz for the 852 nm and 510 nm lasers, respectively. To reduce the effects of environmental electromagnetic reflections, multipath effects, and spurious signals on atomic detection, the entire optical setup and atomic vapor cell are placed inside a microwave anechoic chamber.

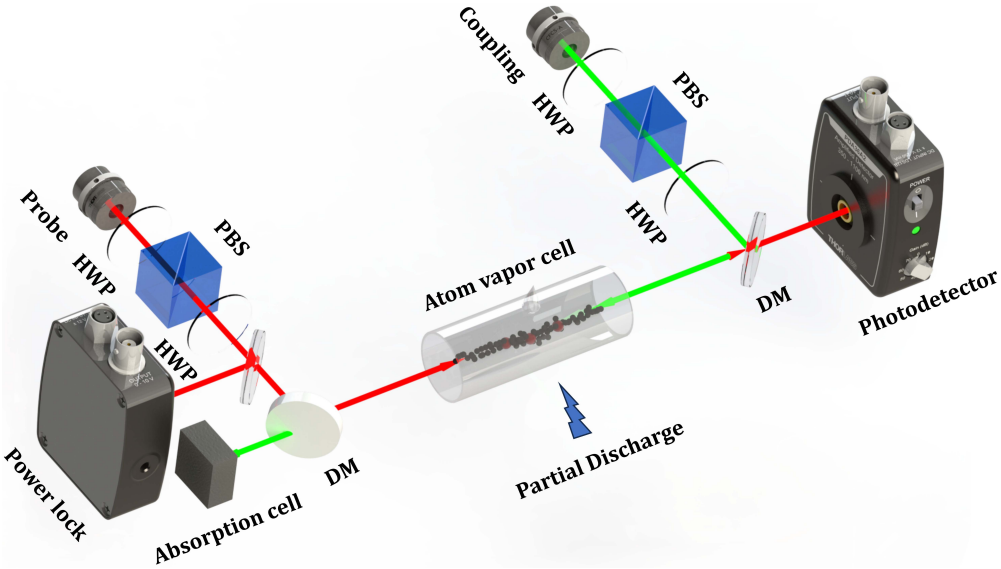


Figure 1. Optical setup of the Rydberg-atom sensor for partial discharge electromagnetic signal detection. The probe and coupling lasers counter-propagate along the same optical axis through the Cs vapor cell, with their frequencies locked to the EIT two-photon resonance. HWP: half-wave plate; PBS: polarizing beam splitter; DM: dichroic mirror.

3.2. Partial Discharge Models

We construct four typical PD models to emulate common insulation-defect discharge behaviors in power systems, as illustrated in Figure 2. Figure 2a shows the metal floating discharge model, which consists of a metal wire–capacitor series structure and a metal plate. The metal wire has a radius of approximately 500 μm, and a 100 nF capacitor is connected in series to emulate the charge accumulation and release processes of floating metallic components under alternating electric fields. The distance between the metal wire and plate electrodes is approximately 0.4 mm. Figure 2b presents the surface creeping discharge model, which adopts a needle–plate configuration with an insulating tape placed between the needle electrode and the metal plate. The gap distance is approximately 5 mm.

Figure 2c depicts the cable air-gap discharge model, formed by two tightly wound cables conforming to the GB/T 19666 standard, with a copper conductor cross-sectional area of 1.5 mm^2. Figure 2d shows the corona discharge model, which consists of a needle–plate electrode configuration. The curvature radius of the needle tip is approximately 300 μm, and the gap distance between the needle and plate electrodes is 5 mm. The PD models are positioned at the same height as the cesium vapor cell, with a horizontal separation of approximately 5 cm. A 50 Hz, 2.5 kV high-voltage supply is applied across the electrodes to generate the PD signals.

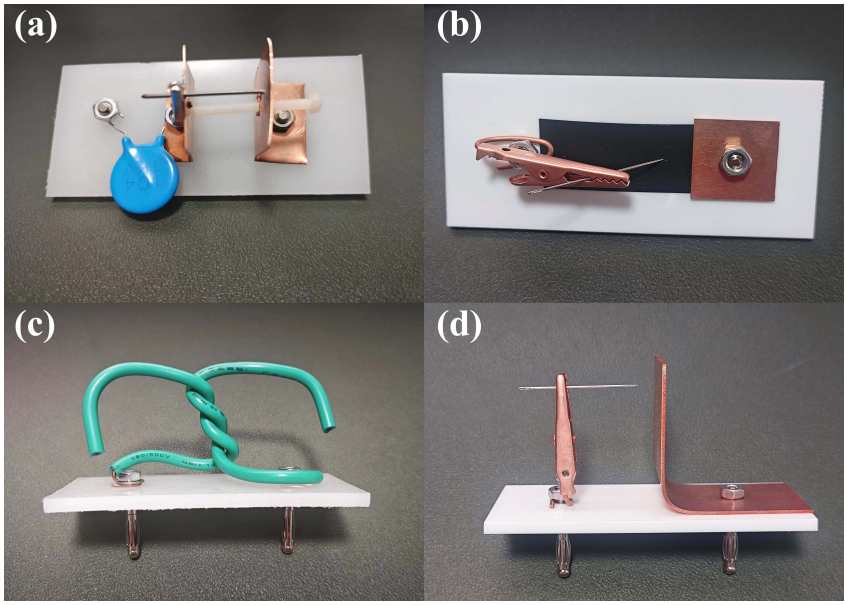


Figure 2. Experimental setups of the four partial discharge models used in this study. (**a**) Metal floating discharge; (**b**) insulation surface creeping discharge; (**c**) cable air-gap discharge; (**d**) corona discharge.

3.3. Sensors

The three sensors used in the experiment are shown in Figure 3. Figure 3a shows the cesium vapor cell, which is a sealed cylindrical glass cell with a length of 10 cm and a diameter of 2 cm. The cell is filled with cesium vapor, and its theoretical measurement bandwidth can cover the DC–THz frequency range. Figure 3b shows the UHF sensor (TWUHF-G04, Tianwei Xinyu), which has a measurement bandwidth of 0.3–1.5 GHz and a detection sensitivity of 1 pC. Figure 3c shows the custom-built monopole antenna, with a measurement bandwidth of approximately 0.29–3.16 GHz [31].

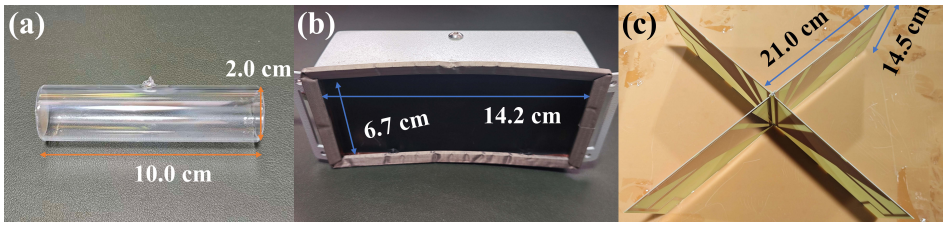


Figure 3. Three sensors used for partial discharge electromagnetic signal detection: (**a**) Rydberg-atom sensor, (**b**) commercial UHF sensor, and (**c**) custom-built monopole antenna.

4. Results

Figure 4 shows the typical time-domain responses of four types of partial discharge signals acquired by the Rydberg-atom sensor within a 20 ms time window. Since 20 ms corresponds exactly to one power-frequency cycle, this time window captures the transient

responses of the partial discharges over one complete cycle. To examine the response of the Rydberg-atom sensor to discharge signals in the lower-frequency range, the signals shown in the figure are processed using a 100 kHz low-pass filter. The filtered signals still exhibit clear transient intensity variations, with differences among the four discharge types in pulse amplitude, occurrence frequency, and temporal distribution. In particular, some pulses from the metal floating discharge exhibit relatively large amplitudes, whereas the pulse amplitudes of the insulation surface creeping, cable air-gap, and corona discharges are generally at a similar level, with relatively dense pulse sequences. The Rydberg-atom sensor can thus capture the transient responses of different types of partial discharges under 100 kHz low-pass filtering, demonstrating its response to discharge signals in the lower-frequency range and providing a basis for further comparison of the PD information obtained using different sensing approaches.

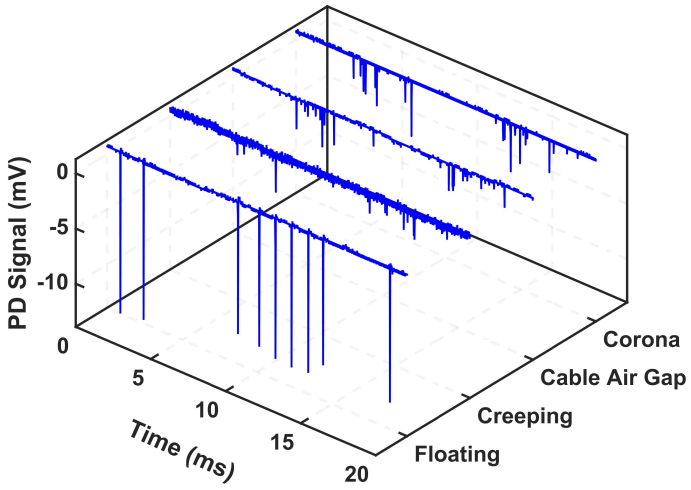


Figure 4. Typical time-domain responses of four types of partial discharge signals measured by the Rydberg-atom sensor after 100 kHz low-pass filtering. The labels floating, creeping, cable air-gap, and corona correspond to metal floating discharge, surface creeping discharge, cable air-gap discharge, and corona discharge, respectively. The negative-going pulses indicate decreases in transmitted probe-light intensity relative to the EIT peak intensity and do not directly represent the polarity of the PD electromagnetic signals.

These results show that the Rydberg-atom sensor can convert the transient electromagnetic disturbances generated by partial discharges into measurable optical intensity variations and capture discharge responses with distinct temporal characteristics. To further examine the correspondence between the discharge pulses of the four PD types and the phase of the applied AC voltage, 10 s of PD signals containing approximately 500 power-frequency cycles are acquired for constructing the PRPD patterns. The signals are likewise processed using a 100 kHz low-pass filter. The time-domain signals are first converted to their absolute values, and the peak positions of the discharge pulses are extracted using peak detection. The power-frequency cycle is then determined from the synchronization signal obtained from the power supply, and the corresponding phase of each discharge pulse is calculated. The discharge pulses are subsequently mapped onto the corresponding phase intervals to obtain the PRPD patterns for the four PD types as shown in Figure 5.

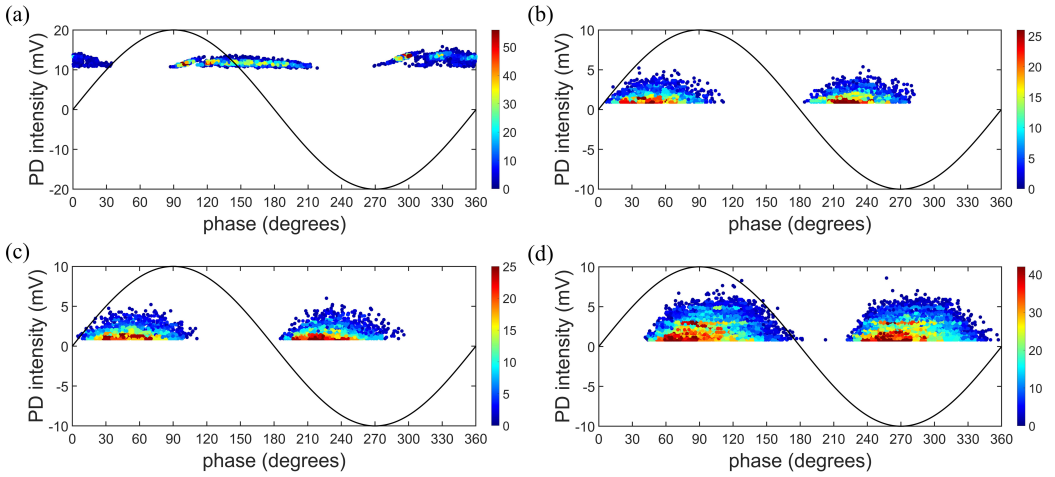


Figure 5. PRPD patterns of four types of partial discharge signals measured by the Rydberg-atom sensor after 100 kHz low-pass filtering: (**a**) metal floating discharge, (**b**) insulation surface creeping discharge, (**c**) cable air-gap discharge, and (**d**) corona discharge.

The PRPD patterns show that the discharge signals from the metal floating discharge are mainly concentrated in the phase ranges of 90–210°, 300–360°, and 0–30°. The signals from the insulation surface creeping and cable air-gap discharges are mainly distributed in the phase ranges of 0–90° and 180–270°. In contrast, the corona discharge signals are mainly concentrated in the phase ranges of 45–150° and 225–330°. It should be noted that the discharge signals from the corona discharge in the 45–150° phase range mainly correspond to transient discharge activity occurring during the breakdown process of the corona discharge.

To further compare the responses of different sensing approaches to PD electromagnetic signals, we measure the four types of PD under the same experimental conditions but without filtering, using a commercial UHF sensor. The corresponding time-domain signals are shown in Figure 6. Unlike the optical intensity response of the Rydberg-atom sensor, the UHF sensor directly measures the high-frequency electromagnetic response generated by PD, and its output signal can therefore exhibit both positive and negative variations. The pulse amplitudes and polarity variations differ to some extent among the different PD types, among which the metal floating discharge signal has a significantly higher amplitude than the other discharge types. To present all discharge signals within the same vertical scale, its amplitude is reduced by a factor of 10 in the figure.

On this basis, 10 s of UHF PD signals are acquired, and the same PRPD processing procedure is applied to obtain the PRPD patterns of the four PD types as shown in Figure 7. The PRPD phase distributions obtained with the UHF sensor are generally consistent with those obtained with the Rydberg-atom sensor, with all four PD types exhibiting similar major phase-distribution characteristics.

The time-domain signals of the four types of partial discharge measured using the custom-built monopole antenna are shown in Figure 8. These signals are likewise acquired without low-pass filtering. Similar to the UHF sensor, the signals measured by the monopole antenna also exhibit both positive and negative variations. Likewise, because the amplitude of the metal floating discharge signal is significantly higher than those of the other discharge types, its amplitude is reduced by a factor of 10 in the figure to facilitate the presentation of all discharge signals within the same vertical scale.

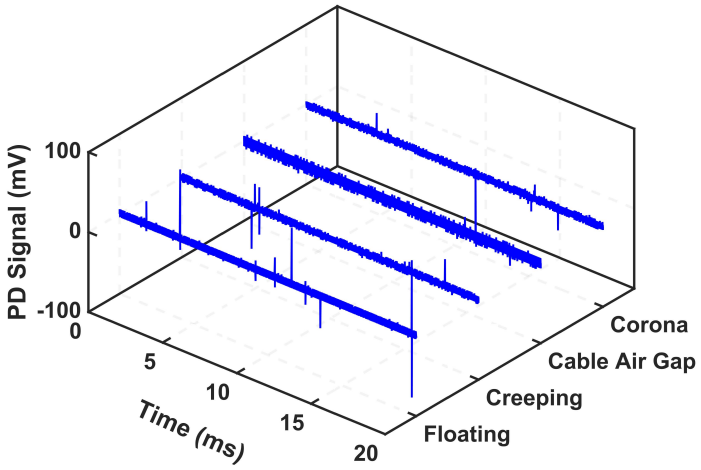


Figure 6. Typical time-domain responses of four types of partial discharge signals measured by the UHF sensor. The amplitude of the metal floating discharge signal is reduced by a factor of 10 for display.

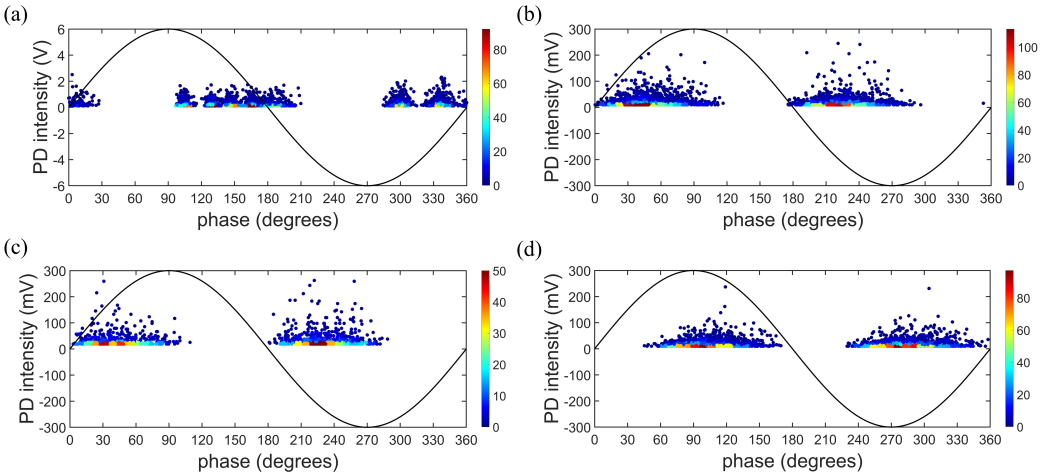


Figure 7. PRPD patterns of four types of partial discharge signals measured by the commercial UHF sensor: (**a**) metal floating discharge, (**b**) insulation surface creeping discharge, (**c**) cable air-gap discharge, and (**d**) corona discharge.

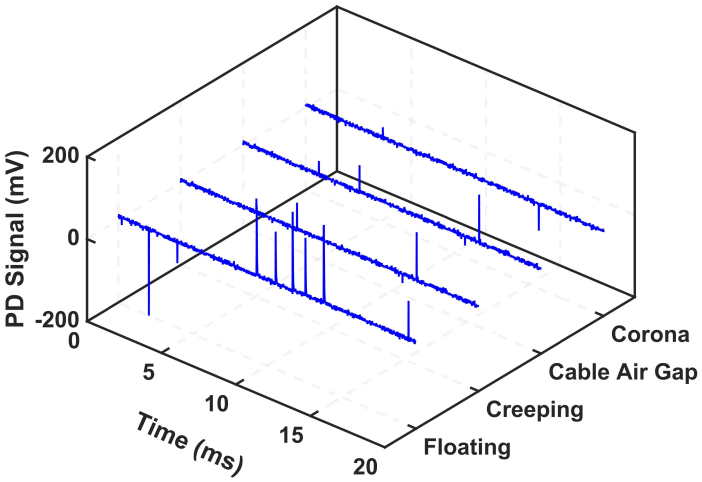


Figure 8. Typical time-domain responses of four types of partial discharge signals measured by the custom-built monopole antenna. The amplitude of the metal floating discharge signal is reduced by a factor of 10 for display.

The PRPD patterns obtained using the same data-processing procedure are shown in Figure 9. The phase distributions of the four PD types are generally consistent with those obtained using the two sensing approaches described above, although differences can be observed in the signal density and amplitude distribution.

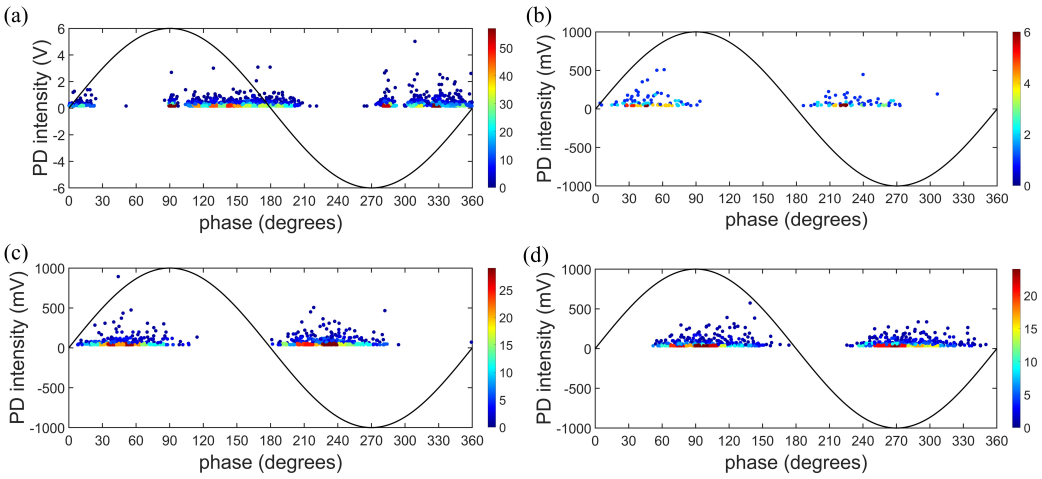


Figure 9. PRPD patterns of four types of partial discharge signals measured by the custom-built monopole antenna: (**a**) metal floating discharge, (**b**) insulation surface creeping discharge, (**c**) cable air-gap discharge, and (**d**) corona discharge.

Taken together, all three approaches capture the four PD types under their respective measurement conditions, with consistent PRPD phase distributions. The relative amplitude trend is also similar across the three approaches, with the metal floating discharge exhibiting a higher output amplitude than the other three PD types. In addition, under the same 100 kHz low-pass filtering, only the Rydberg-atom sensor retains clear transient responses.

5. Discussion

The three sensing approaches employ different physical principles and produce different types of output signals. The Rydberg-atom sensor detects the electric field by monitoring the EIT-induced change in transmitted probe-light intensity. The PD signal is therefore converted into an optical intensity change, and its maximum variation is inherently bounded by the EIT peak intensity (approximately 20 mV in our setup). In the present measurements, the signal variation does not reach this upper bound. In contrast, the commercial UHF sensor and the custom-built monopole antenna directly convert the PD electromagnetic field into a voltage signal and can be further amplified. Because the three approaches have different sensing mechanisms and detection chains, their absolute output amplitudes cannot be directly compared quantitatively without appropriate calibration. Nevertheless, all three approaches exhibit the same relative amplitude trend within their respective measurements, with the metal floating discharge showing the highest amplitude among the four PD types. For the metal floating discharge, charge accumulates on the isolated metal part until the potential difference reaches the breakdown threshold, after which the accumulated charge is released in a single discharge event, producing a larger transient current and stronger electromagnetic radiation than the other discharge types [32].

The differences observed after low-pass filtering can be attributed to the distinct sensing mechanisms and effective bandwidths of the three approaches. The commercial UHF sensor and the custom-built monopole antenna are metal-antenna-based devices that rely on electromagnetic coupling and resonance, and their effective bandwidths are typically located in the high-frequency range. When a 100 kHz low-pass filter is applied, the high-frequency components of the PD signals are largely removed, and the remaining low-

frequency components fall outside the effective bandwidths of these antennas, leading to no obvious discharge response. In contrast, the Rydberg-atom sensor measures the electric field through atomic energy-level transitions and optical detection, without relying on a metallic antenna structure. Its response is therefore not limited by antenna resonance and can remain sensitive to low-frequency electric-field variations, which explains why clear transient PD responses are still observed after low-pass filtering. The consistency in the main PRPD phase distributions indicates that all three approaches capture the same underlying PD phase characteristics, while the differences in pulse amplitude, pulse density, and waveform reflect their different frequency responses and sensitivities. The Rydberg-atom sensor thus provides complementary low-frequency information that is difficult to obtain with conventional UHF and antenna-based measurements.

6. Conclusions and Outlook

In this work, Rydberg-atom sensing was applied to the characterization of partial discharge electromagnetic signals and compared with a commercial UHF sensor and a custom-built monopole antenna. The results show that Rydberg-atom sensing can obtain phase information of partial discharge signals consistent with that obtained using conventional electromagnetic sensing approaches. In addition, clear transient discharge responses remain observable from the Rydberg-atom sensor after 100 kHz low-pass filtering, indicating its response to lower-frequency information contained in partial discharge signals. Therefore, Rydberg-atom sensing can complement conventional UHF and antenna measurements and provide an additional approach for characterizing partial discharge electromagnetic signals over different frequency components.

However, the investigation of lower-frequency information in this work is mainly based on the low-pass-filtered results obtained with the Rydberg-atom sensor, and a direct and quantitative comparison of the frequency responses of the three sensing approaches under the same conditions has not yet been performed. Future work could employ controllable electromagnetic field sources to systematically characterize the responses of the three sensing approaches at different frequencies, and further compare their response amplitudes, sensitivities, and noise levels. From an application perspective, Rydberg-atom sensing relies on an atomic vapor cell and optical detection for electric-field measurement, and its sensing element does not require a conventional metal antenna structure. Therefore, future work could achieve a miniaturized all-optical design, which is expected to be deployed inside enclosed equipment such as switchgear or at specific locations within gas insulated switchgear (GIS) for online partial discharge monitoring.

Author Contributions: H.Z. (Haofeng Zhang): Conceptualization (supporting), methodology (lead), investigation (lead), and validation (lead). Writing—original draft(equal). J.C.: Data curation (lead), formal analysis (lead), investigation (lead), visualization (lead), and writing—original draft (equal). H.Z. (Hao Zhang): Conceptualization (equal), funding acquisition (supporting), project administration (lead), supervision (lead), and writing—review and editing (equal). B.L.: Conceptualization(equal), Writing—review and editing (equal), supervision (equal), project administration (equal). W.Y.: Methodology (supporting) and writing—review and editing (supporting). M.J.: Supervision (supporting). Z.L.: Funding acquisition (equal), methodology (supporting), and supervision (supporting). J.X.: Funding acquisition (equal), methodology (supporting), and supervision (supporting). L.Z.: Conceptualization (supporting), funding acquisition (equal), project administration (equal), and supervision (equal). L.X.: Funding acquisition (supporting), project administration (supporting), and supervision (supporting). S.J.: Project administration (supporting) and supervision (supporting). All authors have read and agreed to the published version of the manuscript.

Funding: This research was funded by "National Engineering Research Center of UHV Technology and New Electrical Equipment Basis. grant number NERCUHE-2024-KF-01".

Data Availability Statement: The data that support the findings of this study are not publicly available at the time of publishing this article but can be obtained from the corresponding author upon reasonable request.

Acknowledgments: We thank engineer Guowei Li from Foshan Power Supply Bureau of Guangdong Power Grid Co., Ltd. for insightful discussions about the theme of partial discharge.

Conflicts of Interest: Authors Haofeng Zhang and Bing Luo are the employees of China Southern Power Grid, Guangzhou 510000, China. The authors declare no conflicts of interest.

References

1. Habib, B.; Zaabi, O.A.; Harid, N.; Hosani, K.A.; Alkhatib, M. Condition Monitoring Based on Partial Discharge Diagnostics Using UHF Sensors: A Comprehensive State-of-the-Art Review. *IEEE Trans. Dielectr. Electr. Insul.* **2024**, *31*, 2860–2873. [CrossRef]
2. Hussain, G.A.; Hassan, W.; Mahmood, F.; Shafiq, M.; Rehman, H.; Kay, J.A. Review on Partial Discharge Diagnostic Techniques for High Voltage Equipment in Power Systems. *IEEE Access* **2023**, *11*, 51382–51394. [CrossRef]
3. Hassan, W.; Shafiq, M.; Hussain, G.A.; Choudhary, M.; Palu, I. Investigating the Progression of Insulation Degradation in Power Cable Based on Partial Discharge Measurements. *Electr. Power Syst. Res.* **2023**, *221*, 109452. [CrossRef]
4. Bartnikas, R. Partial Discharges. Their Mechanism, Detection and Measurement. *IEEE Trans. Dielectr. Electr. Insul.* **2002**, *9*, 763–808. [CrossRef]
5. Montanari, G.C.; Myneni, S.B.; Chen, Z.; Shafiq, M. Sensing and Analyzing Partial Discharge Phenomenology in Electrical Asset Components Supplied by Distorted AC Waveform. *Sensors* **2025**, *25*, 6594. [CrossRef] [PubMed]
6. Faizol, Z.; Zubir, F.; Saman, N.M.; Ahmad, M.H.; Rahim, M.K.A.; Ayop, O.; Jusoh, M.; Majid, H.A.; Yusoff, Z. Detection Method of Partial Discharge on Transformer and Gas-Insulated Switchgear: A Review. *Appl. Sci.* **2023**, *13*, 9605. [CrossRef]
7. Chai, H.; Phung, B.T.; Mitchell, S. Application of UHF Sensors in Power System Equipment for Partial Discharge Detection: A Review. *Sensors* **2019**, *19*, 1029. [CrossRef] [PubMed]
8. *IEC 60270*; High-Voltage Test Techniques—Partial Discharge Measurements. International Electrotechnical Commission: Geneva, Switzerland, 2025. Available online: https://webstore.iec.ch/en/publication/65087 (accessed on 7 October 2026).
9. Tenbohlen, S.; Denissov, D.; Hoek, S.M.; Markalous, S.M. Partial Discharge Measurement in the Ultra High Frequency (UHF) Range. *IEEE Trans. Dielectr. Electr. Insul.* **2008**, *15*, 1544–1552. [CrossRef]
10. Bandi, T.; Ohtsuka, S. Partial Discharge Detection of Multiple-Narrow Band Antenna under the Radio Communication Noise. *IEEJ Trans. Electr. Electron. Eng.* **2021**, *16*, 715–721. [CrossRef]
11. Mohammadi, H.; Haghjoo, F. Feasibility Study for Partial Discharge Detection and Defective Region Identification in Power Transformers by Using Distributed Sensors. *IET Gener. Transm. Distrib.* **2016**, *10*, 4006–4023. [CrossRef]
12. Pattanadech, N.; Haller, R.; Kornhuber, S.; Muhr, M. Electromagnetic Methods for PD Detection. In *Partial Discharges (PD)*; Wiley: Hoboken, NJ, USA, 2023. [CrossRef]
13. *IEC TS 62478*; High Voltage Test Techniques—Partial Discharge Measurements by Electromagnetic and Acoustic Methods. International Electrotechnical Commission: Geneva, Switzerland, 2016. Available online: https://webstore.iec.ch/en/publication/25740 (accessed on 7 October 2026).
14. Robles, G.; Fresno, J.M.; Martínez-Tarifa, J.M.; Ardila-Rey, J.A.; Parrado-Hernández, E. Partial Discharge Spectral Characterization in HF, VHF and UHF Bands Using Particle Swarm Optimization. *Sensors* **2018**, *18*, 746. [CrossRef] [PubMed]
15. Holloway, C.L.; Gordon, J.A.; Jefferts, S.; Schwarzkopf, A.; Anderson, D.A.; Miller, S.A.; Thaicharoen, N.; Raithel, G. Broadband Rydberg Atom-Based Electric-Field Probe for SI-Traceable, Self-Calibrated Measurements. *IEEE Trans. Antennas Propag.* **2014**, *62*, 6169–6182. [CrossRef]
16. Schlossberger, N.; Prajapati, N.; Berweger, S.; Rotunno, A.P.; Artusio-Glimpse, A.B.; Simons, M.T.; Sheikh, A.A.; Norrgard, E.B.; Eckel, S.P.; Holloway, C.L. Rydberg States of Alkali Atoms in Atomic Vapour as SI-Traceable Field Probes and Communications Receivers. *Nat. Rev. Phys.* **2024**, *6*, 606–620. Correction in *Nat. Rev. Phys.* **2024**, *6*, 705. [CrossRef]
17. Zhang, H.; Ma, Y.; Liao, K.; Yang, W.; Liu, Z.; Ding, D.; Yan, H.; Li, W.; Zhang, L. Rydberg Atom Electric Field Sensing for Metrology, Communication and Hybrid Quantum Systems. *Sci. Bull.* **2024**, *69*, 1515–1535. [CrossRef] [PubMed]
18. Anderson, D.A.; Sapiro, R.E.; Raithel, G. A Self-Calibrated SI-Traceable Rydberg Atom-Based Radio Frequency Electric Field Probe and Measurement Instrument. *IEEE Trans. Antennas Propag.* **2021**, *69*, 5931–5941. [CrossRef]
19. Schmidt, M.; Bohaichuk, S.; Venu, V.; Christaller, F.; Liu, C.; Ripka, F.; Kübler, H.; Shaffer, J.P. Rydberg-Atom-Based Radio-Frequency Sensors: Amplitude-Regime Sensing. *Opt. Express* **2024**, *32*, 27768–27791. [CrossRef] [PubMed]
20. Li, L.; Jiao, Y.; Hu, J.; Li, H.; Shi, M.; Zhao, J.; Jia, S. Super Low-Frequency Electric Field Measurement Based on Rydberg Atoms. *Opt. Express* **2023**, *31*, 29228–29234. [CrossRef] [PubMed]

21. Han, M.; Hao, H.; Song, X.; Yin, Z.; Parniak, M.; Jia, Z.; Peng, Y. Microwave Electrometry with Bichromatic Electromagnetically Induced Transparency in Rydberg Atoms. *EPJ Quantum Technol.* **2023**, *10*, 28. [CrossRef]
22. Prajapati, N.; Long, D.A.; Artusio-Glimpse, A.B.; Bresler, S.M.; Holloway, C.L. Multichannel, Ultra-Wideband Rydberg Electrometry with an Optical Frequency Comb. *Nat. Commun.* **2025**, *16*, 11054. [CrossRef] [PubMed]
23. Wang, E.-H.; Wang, Q.-F.; Geng, J.-Q.; Tian, T.; Qiu, R.-J.; Xue, B.; Yuan, Y.-W.; Zhao, L.; Ding, D.-S. Investigation of Partial Discharge Detection Based on Rydberg-Atom Electric Field Sensing. *Chin. Phys. B* **2025**, *35*, 104209 . [CrossRef]
24. Wang, Q.-F.; Zhang, L.-H.; Liu, B.; Ma, Y.; Han, T.-Y.; Wang, E.-H.; Zhang, Z.-Y.; Shao, S.-Y.; Zhang, J.; Li, Q.; et al. Measurement of Arc RF Signals Based on Rydberg Atoms. *Phys. Rev. Appl.* **2025**, *24*, 014006. [CrossRef]
25. Yuan, H.; Luo, B.; Chen, J.; Zhang, L.; Zhang, H.; Yang, W.; Zhang, L.; Zhang, H. Corona Discharge Signal Measurement Based on Rydberg Atoms. *Chin. J. Quantum Electron.* **2025**, *42*, 556–564. [CrossRef]
26. Abubakar, A.; Zachariades, C. Phase-Resolved Partial Discharge (PRPD) Pattern Recognition Using Image Processing Template Matching. *Sensors* **2024**, *24*, 3565. [CrossRef] [PubMed]
27. Lee, G.-Y.; Kim, N.-H.; Kim, D.-E.; Kil, G.-S.; Kim, S.-W. The Design, Fabrication, and Evaluation of a Phase-Resolved Partial Discharge Sensor Embedded in a MV-Class Bushing. *Sensors* **2023**, *23*, 9844. [CrossRef] [PubMed]
28. Kaziz, S.; Hadj Said, M.; Imburgia, A.; Maamer, B.; Flandre, D.; Romano, P.; Tounsi, F. Radiometric Partial Discharge Detection: A Review. *Energies* **2023**, *16*, 1978. [CrossRef]
29. Ilkhechi, H.D.; Samimi, M.H.; Yousefvand, R. Generation of Acoustic Phase-Resolved Partial Discharge Patterns by Utilizing UHF Signals. *Int. J. Electr. Power Energy Syst.* **2019**, *113*, 906–915. [CrossRef]
30. Drever, R.W.P.; Hall, J.L.; Kowalski, F.V.; Hough, J.; Ford, G.M.; Munley, A.J.; Ward, H. Laser Phase and Frequency Stabilization Using an Optical Resonator. *Appl. Phys. B* **1983**, *31*, 97–105. [CrossRef]
31. Zhang, Y.; Luo, B.; Li, G. An Ultra-Wideband Loop-Monopole Antenna for Partial Discharge Detection. *Electron. Components Mater.* **2024**, *43*, 1017–1023.. [CrossRef]
32. Khayam, U.; Putro, W.; Sriyono, S.; Urano, K.; Min, C.; Harjo, S.; Kozako, M.; Hikita, M. Partial Discharge Pattern of Various Defects Measured by Spiral Antenna as UHF External Sensor on 66 kV GIS Model. *Int. J. Electr. Eng. Inform.* **2014**, *6*, 404–420. [CrossRef]

Disclaimer/Publisher's Note: The statements, opinions and data contained in all publications are solely those of the individual author(s) and contributor(s) and not of MDPI and/or the editor(s). MDPI and/or the editor(s) disclaim responsibility for any injury to people or property resulting from any ideas, methods, instructions or products referred to in the content.